Low-loss composite photonic platform based on 2D semiconductor monolayers

Ipshita Datta[1,*], Sang Hoon Chae[2,*], Gaurang R. Bhatt[1], Mohammad A. Tadayon[1], Baichang Li[2], Yiling Yu[3], Chibeom Park[4], Jiwoong Park[4], Linyou Cao[3], D. N. Basov[5], James Hone[2] and Michal Lipson[1]

[1]Department of Electrical Engineering, Columbia University, New York, New York 10027, USA

[2]Department of Mechanical Engineering, Columbia University, New York, New York 10027, USA

[3]Department of Materials Science and Engineering and Department of Physics, North Carolina State University, Raleigh, North Carolina 27695, USA

[4]Department of Chemistry, Institute for Molecular Engineering, James Franck Institute, University of Chicago, Chicago, IL 60637, USA

[5]Department of Physics, Columbia University, New York, New York 10027, USA

Corresponding Author – ml3745@columbia.edu

*These authors contributed equally to this work.

Two dimensional (2D) materials such as graphene and transition metal dichalcogenides (TMDs) are promising for optical modulation, detection, and light emission since their material properties can be tuned on-demand via electrostatic doping[1–21]. The optical properties of TMDs have been shown to change drastically with doping in the wavelength range near the excitonic resonances[22–26]. However, little is known about the effect of doping on the optical properties of TMDs away from these resonances, where the material is transparent and therefore could be leveraged in photonic circuits. Here, we probe the electro-optic response of monolayer TMDs at near infrared (NIR) wavelengths (i.e. deep in the transparency regime), by integrating them on silicon nitride (SiN) photonic structures to induce strong light -matter interaction with the monolayer. We dope the monolayer to carrier densities of $(7.2 \pm 0.8) \times 10^{13}$ cm^{-2}, by electrically gating the TMD using an ionic liquid [P14$^+$] [FAP$^-$]. We show strong electro-refractive response in monolayer tungsten disulphide (WS$_2$) at NIR wavelengths by measuring a large change in the real part of refractive index $\Delta n = 0.53$, with only a minimal change in the imaginary part $\Delta k = 0.004$. We demonstrate photonic devices based on electrostatically gated SiN-WS$_2$ phase modulator with high efficiency ($V_\pi L$) of 0.8 V · cm. We show that the induced phase change relative to the change in absorption (i.e. $\Delta n/\Delta k$) is approximately 125, that is significantly higher than the ones achieved in 2D materials at different spectral ranges and in bulk materials, commonly employed for silicon photonic modulators such as Si and III-V

on Si, while accompanied by negligible insertion loss. Efficient phase modulators are critical for enabling large-scale photonic systems for applications such as Light Detection and Ranging (LIDAR), phased arrays, optical switching, coherent optical communication and quantum and optical neural networks[27–30].

In order to probe the doping induced electro-optic response of TMDs, we utilize a SiN-TMD composite waveguide platform in which the optical mode of the composite waveguide is shared between the TMD monolayer and the dielectric SiN waveguide. These waveguides are then incorporated into photonic structures such as microring resonators which are sensitive to small changes in absorption and phase induced by electrostatic doping of the TMD monolayer. The SiO_2-clad SiN waveguides are fabricated using standard techniques, and then planarized to permit mechanical transfer of TMD layers and subsequent lithographic patterning to define Ti/Au contacts for gating (see Methods)[21]. We probe the response of these structures in the NIR region ($\lambda \sim 1550$ nm), far below the excitonic resonances of the TMDs (~ 620 nm for WS_2; 660 nm for MoS_2).

We first characterize the electro-optic response of monolayer WS_2 by measuring the effect of gating on the response of a microring resonator cavity (1.3 μm × 330 nm passive SiN waveguide clad with 100 nm of SiO_2, embedded in a ring of 60 µm radius), as depicted in figure 1a. The high-Q ($\sim$120,000) cavity is critically coupled to a SiN bus waveguide, such that the transmission spectrum is extremely sensitive to small changes in phase and absorption within the cavity. A 30 µm arc length of WS_2 grown by metal-organic chemical vapor deposition (MOCVD)[31] is patterned onto the ring and electrically contacted (see Methods). We tune the effective index of the optical mode by electrostatically doping the monolayer using an ionic liquid $[P14^+]$ $[FAP^-]$, chosen due to its stability to gating under atmospheric exposure at room temperature[32]. As shown in figure 1b, we apply a potential difference between the electrode connected to WS_2 and a nearby counter-electrode, which results in the accumulation of ions at the surface of WS_2. We note that ionic liquid gated devices are dominated by the quantum capacitance (C_q)[32], such that no carriers are injected to the WS_2 within the bandgap region (roughly -1 to 1 V). The maximum electron doping density induced in the monolayer is about 7.2 $\pm$ 0.8 x 10^{13} cm^{-2} with an applied voltage of 2 V (see Supplementary Section I). One can see from

65   the cross-section of the platform in figure 1c, that the optical mode is shared between the

66   monolayer and SiN waveguide. We estimate an optical mode overlap of 0.06 % using COMSOL

67   Multiphysics simulations (see Methods).

68

69   Figure 1d shows the measured transmission spectrum of the ring resonator as a function of

70   voltage. The cavity has a resonance near 1571 nm, with narrow linewidth confirming that

71   incorporation of WS_2 introduces negligible loss and does not degrade the quality factor of the

72   microring resonator. At positive gate voltages above 1 V, we observe a red shift in the resonance

73   wavelength, indicating an increase in the effective index of the resonator. Remarkably, the

74   resonance linewidth is largely unchanged, thereby showing that doping does not introduce

75   substantial loss. The measured changes in resonance wavelength and quality factor with applied

76   voltage can be used to derive the changes in real and imaginary components of the effective

77   index (Δn_{eff} and Δk_{eff}, respectively) of the composite waveguide (see Supplementary Section

78   II). Figure 1e shows the measured Δn_{eff} and Δk_{eff} as a function of gate voltage. Δn_{eff} increases

79   linearly with gate voltage with the onset of n-type doping (above 1V). In this same range, Δk_{eff}

80   is almost two orders of magnitude smaller. We can then determine the underlying change in real

81   and imaginary part of the refractive index of WS_2, Δn_{WS2} and Δk_{WS2} respectively by COMSOL

82   modelling of the monolayer as a 2D sheet with optical conductivity[33] σ_S integrated on a SiN

83   waveguide (see Methods). Figure 1f shows Δn_{WS2} and Δk_{WS2} as a function of gate-induced

84   carrier density in the monolayer WS_2. Δn_{WS2} reaches 0.53 ± 0.06 RIU (refractive index units) for

85   maximum doping of $(7.2 \pm 0.8) \times 10^{13}$ cm^{-2}, while Δk_{WS2} is 0.004 ± 0.002. This indicates that

86   monolayer WS_2 has a unique combination of strong electro-refractive response (Δn_{WS2}) and

87   small electro-absorptive response (Δk_{WS2}) at NIR wavelengths, i.e. the propagating light

88   undergoes significant phase change with low optical loss.

89
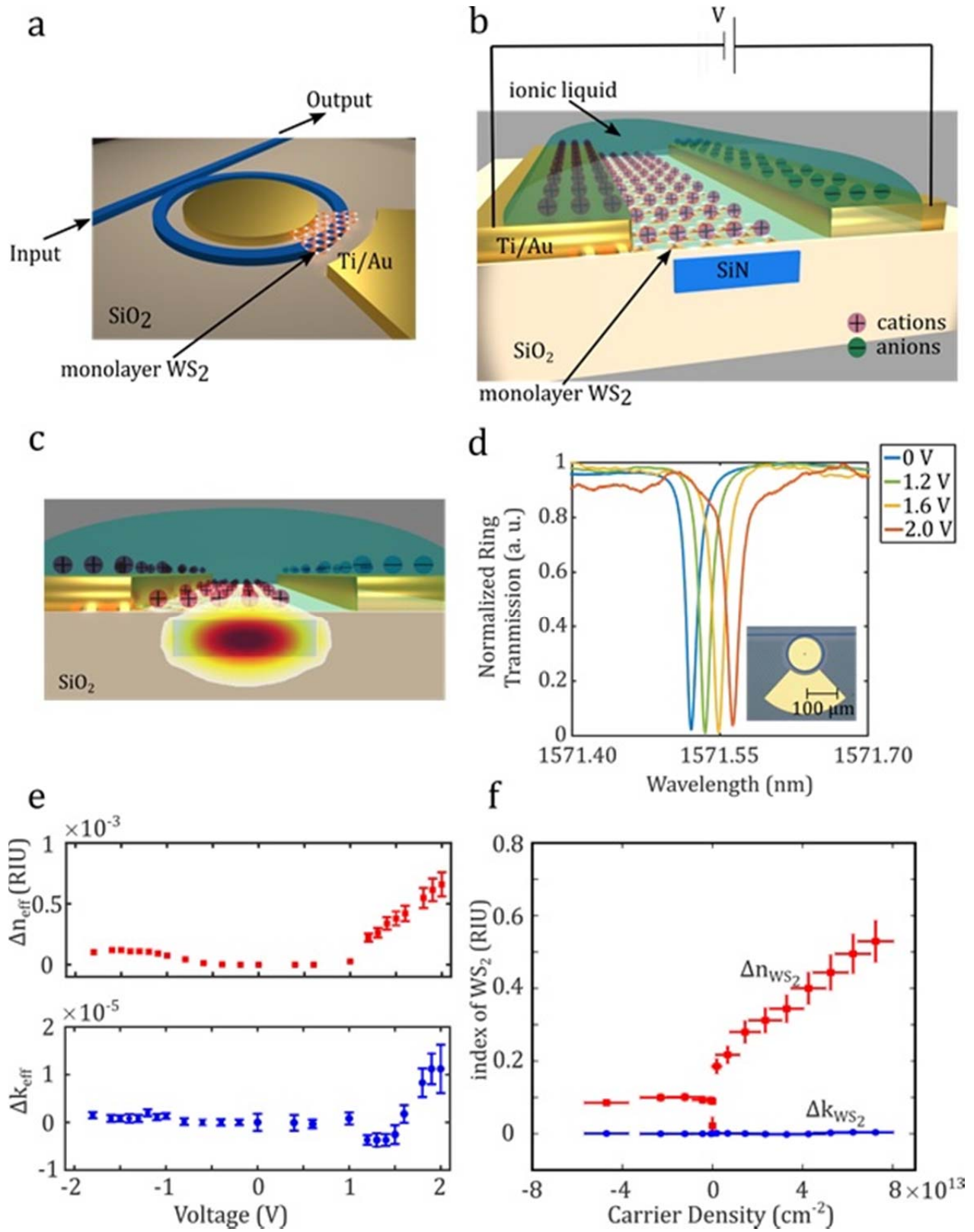
Figure 1 | **Schematic of the ionic liquid gated SiN-WS$_2$ platform.** (a) Schematic representation of a microring resonator with patterned monolayer WS$_2$ and Ti/Au electrodes, in which only one of the electrodes is in contact with

93   the monolayer WS_2. (b) Illustration of the composite SiN-WS_2 waveguide with ionic liquid ([P14$^+$] [FAP$^-$])

94   cladding. The monolayer WS_2 is doped by applying a bias voltage across the two electrodes through the ionic liquid,

95   resulting in the accumulation of charged carriers at the interface of WS_2, thereby creating image charges in the

96   monolayer. (c) TE mode profile of the propagating mode in the SiN waveguide with 0.06 % overlap with monolayer

97   WS_2. (d) Normalized transmission response of the microring resonator for different voltages applied across the two

98   electrodes. One can see that the resonance of the microring red shifts with significantly smaller broadening of the

99   resonance with increasing voltage, indicating that the propagating mode undergoes strong phase shift but with

100   minimal absorption. Bottom right inset is the optical micrograph of the fabricated ring modulator with SiN-WS_2

101   waveguides, before ionic liquid is dispersed on the devices. (e) Change in real and imaginary part of the effective

102   index (Δn_{eff} and Δk_{eff}) of the composite SiN-WS_2 waveguide at different voltages, extracted from the normalized

103   transmission spectra in figure 1d. The error bars shown in figure 1e account for the root mean square (rms) error

104   from the numerical fit and a $\pm$ 5 μm error in the patterned length of the monolayer. (f) Change in the real and

105   imaginary part of the refractive index of monolayer WS_2 (Δn_{WS2} and Δk_{WS2}) with induced carrier densities,

106   extracted from the change in effective index in figure 1e. The vertical error bars in figure 1f incorporates the rms

107   error in the effective index measurements from figure 1e, variation in the thickness of monolayer ($\pm$ 0.05 nm),

108   variation in the height of the cladding oxide by about $\pm$ 25 nm and about $\pm$ 0.02 (RIU) variation in the index of the

109   ionic liquid included during the COMSOL simulations. The horizontal error bars accounts for the error in the

110   intrinsic doping of the monolayer WS_2.

111

112   We show that the strong phase change occurs only when the polarization of the propagating light

113   is in plane with the monolayer TMD (i.e. TE mode). In order to probe the polarization effect, we

114   embed the SiN-WS_2 composite waveguide in the arms of a Mach Zehnder interferometer (MZI),

115   optimized to operate both for the TM and TE mode in the S wavelength band (1460 – 1490 nm)

116   and C/L band (1530 - 1630 nm), respectively (see Methods). Figure 2a illustrates the

117   diagrammatic representation of the MZI device while figure 2b shows an optical micrograph of

118   the fabricated device. The MZI is designed with a length imbalance of 200 μm between the two

119   arms such that the transmission spectra exhibit fringes with a visibility of 0.98 in the wavelength

120   range spanning from 1560 - 1620 nm for TE mode and 1455 - 1480 nm for TM mode. A 500 μm

121   long film of monolayer WS_2 is patterned on both the arms of the MZI, followed by the

122   deposition of metal electrodes. We dope the monolayer by applying a voltage between the metal

123   electrodes through the ionic liquid [P14$^+$] [FAP$^-$]. We estimate from COMSOL Multiphysics

124   simulation that the optical mode overlap with the monolayer is 0.06% and 0.04% for the TE and

125   TM mode, respectively (see Methods). In Figure 2c and 2d, we show the interference pattern at

126   the MZI output for the TE and TM mode, respectively with different voltages applied to dope the

127 monolayer WS$_2$ on the longer arm of the MZI. There is a pronounced wavelength shift in the

128 MZI spectra for the TE mode (Figure 2c), as compared to minimal wavelength shift for the TM

129 mode (Figure 2d), indicating that the doping-induced electro-refractive effect is strong only

130 when the optical E field is aligned with the monolayer, despite similar mode overlap for the

131 TE/TM mode with the monolayer. We further confirm that the doping of ionic liquid in the

132 absence of the monolayer does not influence the MZI transmission response (see Supplementary

133 Section III).

134
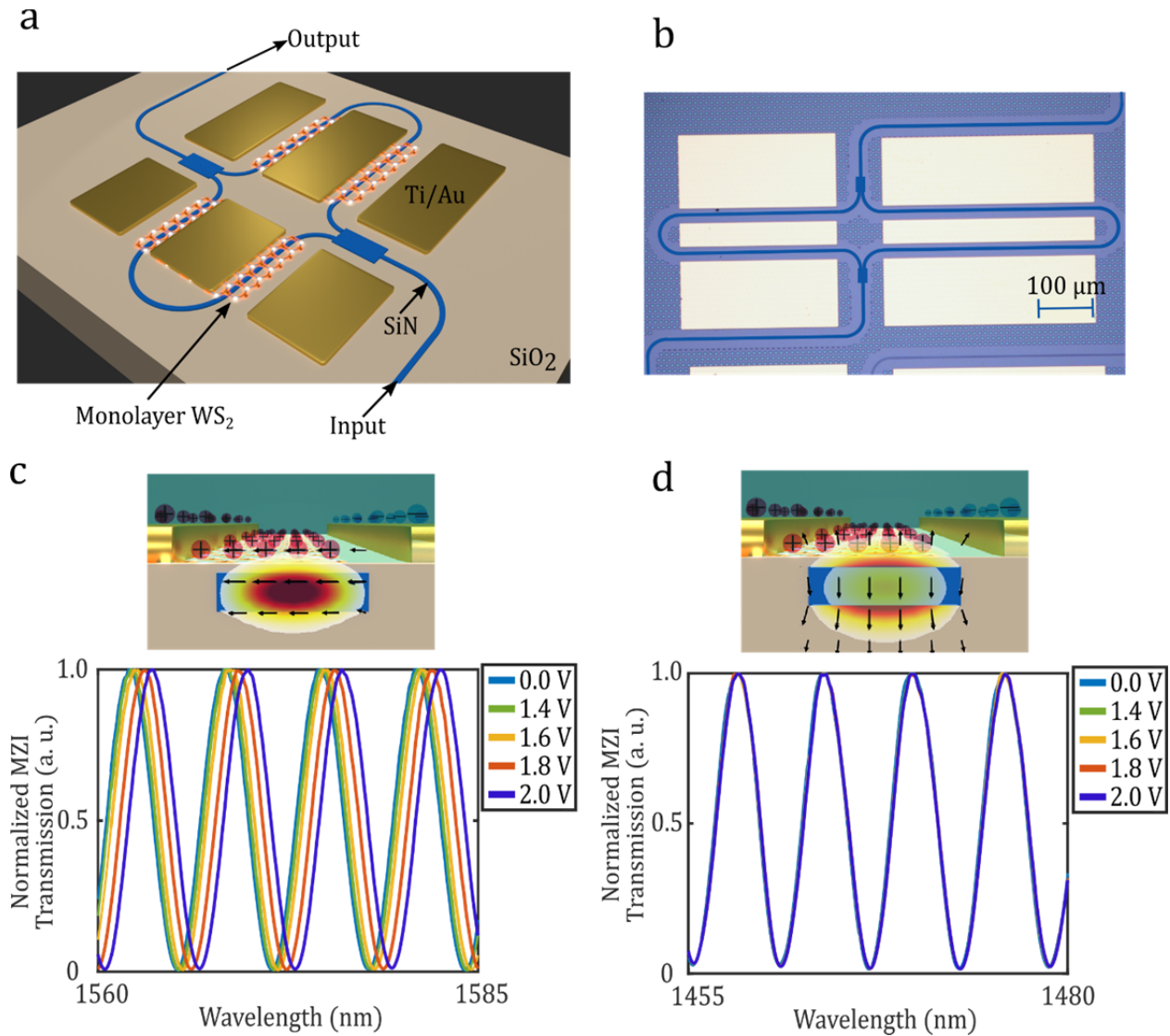
135 **Figure 2 | Tuning the effective index (Δn_{eff}) of the propagating TE and TM mode using monolayer WS$_2$.** (a)

136 Diagrammatic illustration of an on-chip Mach Zehnder interferometer (MZI) with patterned monolayer WS$_2$ on both

137 the arms of MZI. (b) Optical micrograph of the fabricated MZI with SiN-WS$_2$ waveguides, before ionic liquid is

138 dispersed on the devices. (c) Normalized Transmission response of the MZI for the optical TE mode at different

139   voltages applied across the two electrodes located on the longer arm of the MZI. One can see that the MZI

140   transmission spectra exhibit fringes due to the path length difference between the two arms of the MZI, which red

141   shifts with applied voltage. The top figure shows the optical mode profile for the TE mode, with the arrows

142   illustrating the field lines aligned with the plane of monolayer WS_2. (d) Normalized Transmission response of the

143   MZI for the optical TM mode at different voltages. The bottom right inset shows the optical mode profile for the TM

144   mode with the optical field lines perpendicular to the plane of monolayer WS_2.

145

146   To leverage the doping-induced strong electro-refractive response in monolayer TMDs for

147   photonic applications, we develop a fully integrated SiN-TMD platform that gates the monolayer

148   TMD using a parallel plate capacitor configuration. We replace the ionic liquid used above with

149   a stack of HfO_2 (hafnia) and transparent conducting oxide ITO (indium tin oxide) to form the

150   TMD-HfO_2-ITO capacitor on the SiN waveguide, as illustrated in figure 3a. Standard processes

151   are used to define the optimized 1 μm × 360 nm LPCVD SiN waveguide, clad with 260 nm of

152   SiO_2 and a 500 μm long WS_2-HfO_2-ITO capacitor fabricated on each arm of the MZI (see

153   Methods). We replace the MOCVD-grown monolayer WS_2 used in the ionic liquid experiments

154   with CVD-grown[26] films for the capacitive devices (see Supplementary Section IV).

155   Supplementary figure S4a shows the false-coloured optical micrograph of the fabricated SiN-

156   TMD MZI. In this configuration quantum capacitance effects are negligible[32], and we estimate a

157   linear induced charge density of $0.37 \pm 0.05 \times 10^{12}$ cm^{-2} per volt, based on the thickness (26 nm)

158   and dielectric permittivity of the HfO_2. In contrast to the ionic liquid devices where the voltage

159   swing is limited between -2 V to 2 V, the voltage swing in these capacitive devices is determined

160   by the thickness of the dielectric (HfO_2) and is in range of {-8V, 9V}.

161

162   Figure 3b shows the interference pattern at the MZI output for different voltages applied across

163   the WS_2-HfO_2-ITO capacitor on the longer arm of the MZI. As in the ionic liquid gated devices,

164   we induce a strong change in phase with applied voltage, thereby designing a phase modulator

165   with a modulation efficiency ($V_\pi L$) of 1.33 V · cm, coupled with minimal change in extinction.

166   Figure 3c shows the gating induced Δn_{eff} of the composite waveguide, extracted by measuring

167   the wavelength shift of the MZI spectra (see Supplementary Section IV), which reaches 7×10^{-4}

168   RIU for a swing voltage of 8V. From the extremum point at -4 V in Figure 3c, we infer that the

169   charge neutrality point for the monolayer WS_2 layer is at -4 V, which corresponds to an initial

170   electron doping of $1.5 \pm 0.2 \times 10^{12}$ cm^{-2}. This initial doping is likely due to sulfur vacancies
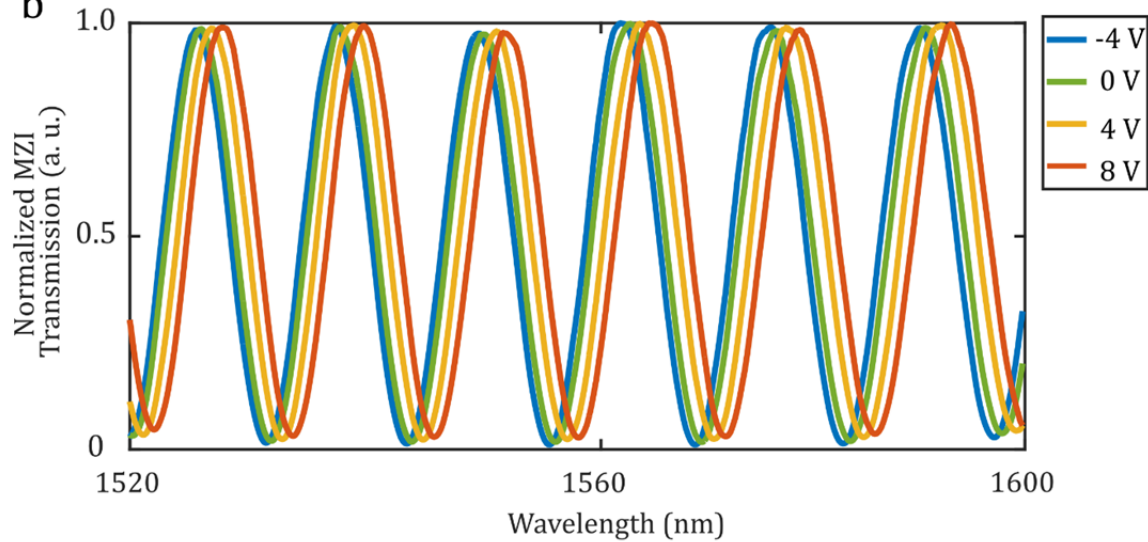
171   arising from CVD growth but can also arise from substrate effects or adsorbates introduced in

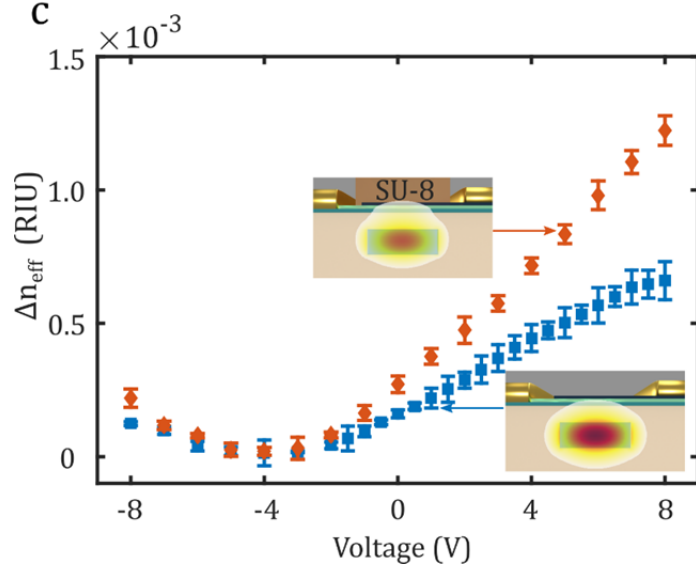172   the transfer process[34].
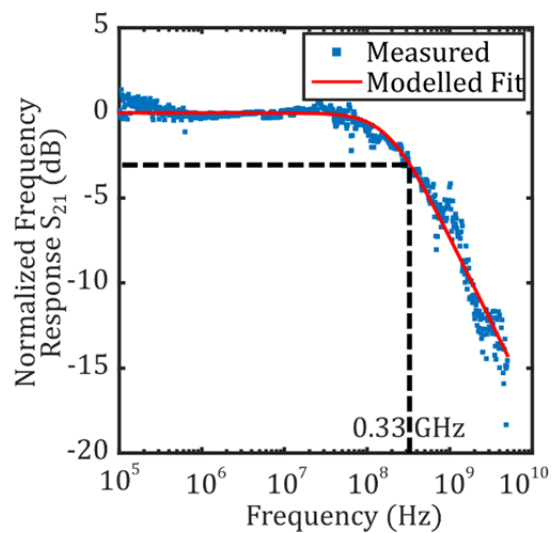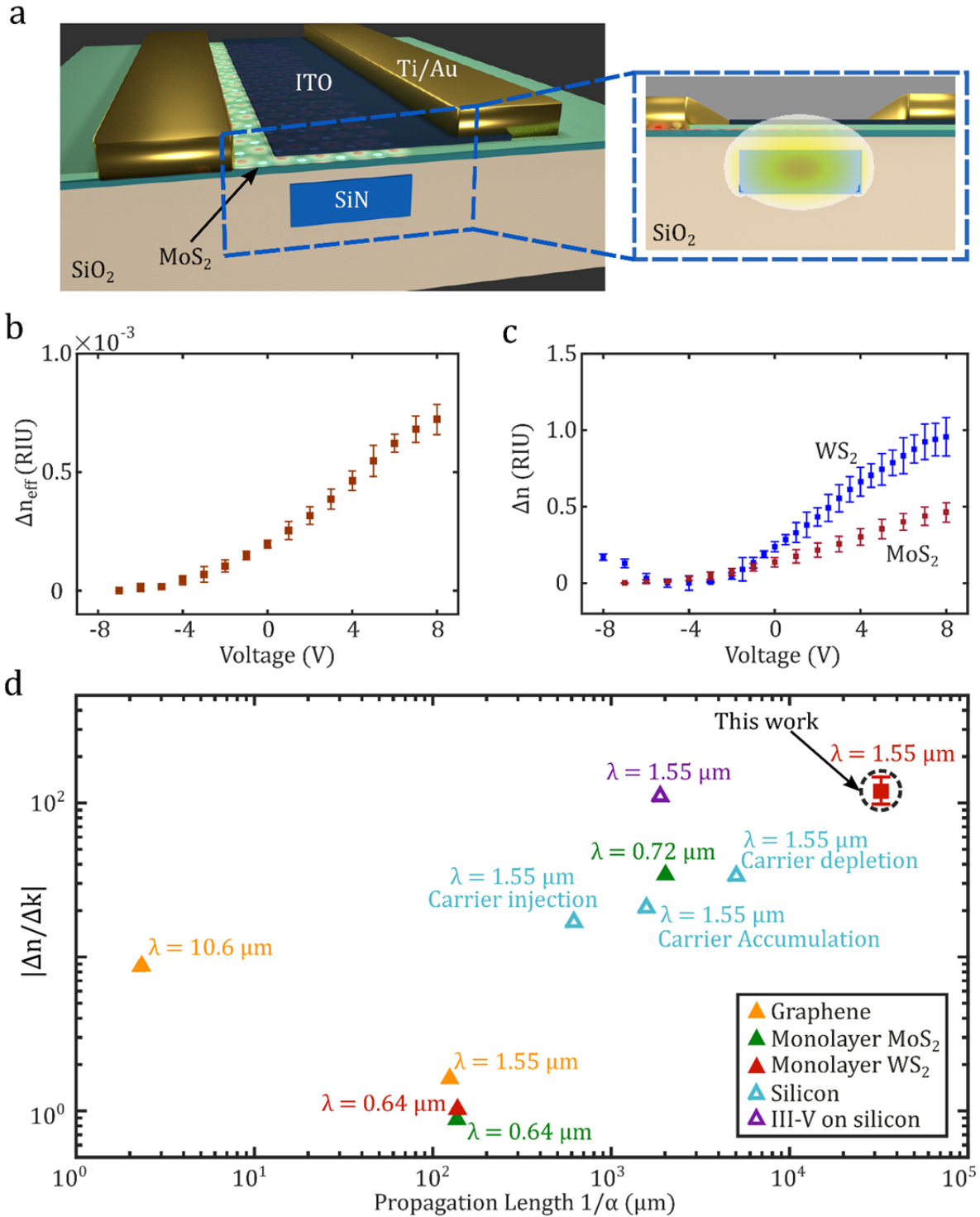

173
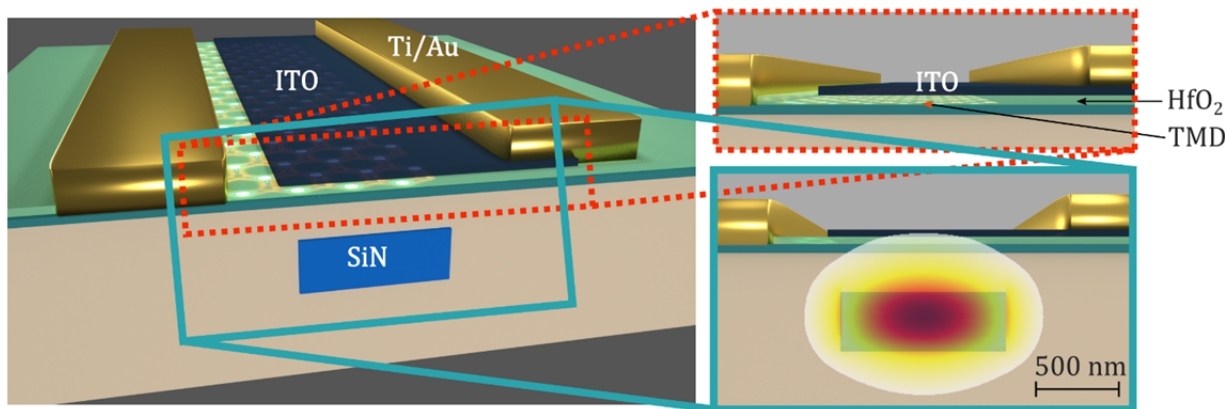
174 **Figure 3| Phase tuning of monolayer TMD using TMD-HfO$_2$-ITO capacitor.** (a) Illustration of a composite SiN-
175 monolayer TMD waveguide, where the optical mode is shared between the SiN waveguide and TMD (bottom right).
176 The top right inset details the TMD-HfO$_2$-ITO parallel plate capacitor configuration which electrostatically dopes
177 the monolayer WS$_2$, by applying a bias voltage between the two electrodes (TMD and ITO) across the dielectric
178 HfO$_2$. (b) Normalized Transmission response of the MZI for different voltages applied across the WS$_2$-HfO$_2$-ITO
179 capacitor. (c) Extracted change in effective index (Δn_{eff}) measured from the MZI spectra of the composite SiN-WS$_2$
180 waveguide with and without SU-8 cladding. The unclad device in figure 3a has a mode overlap of 0.016 % with the
181 monolayer WS$_2$, while the SU-8 clad device has a mode overlap of 0.03 %. One can see that the enhanced mode
182 overlap increases the maximum Δn_{eff} of the composite SiN-WS$_2$ waveguide from 7×10^{-4} to 1.3×10^{-3}
183 (corresponding to a V$_\pi$L of 0.8 V · cm). The error bars show the variation in gating induced Δn_{eff}, extracted from
184 multiple MZI devices with different lengths of WS$_2$-HfO$_2$-ITO capacitor. (d) Frequency response (S$_{21}$) of the unclad
185 SiN-WS$_2$ phase modulator measured at 1550 nm.

187 We further enhance the performance of the capacitive SiN-WS$_2$ platform by increasing the
188 optical mode overlap with monolayer WS$_2$ using SU-8 photoresist as a high index cladding (see
189 Supplementary figure S4b). In figure 3c, we show an increase in the gating induced Δn_{eff} from
190 7.1×10^{-4} RIU to 1.35×10^{-3} RIU which reduces the V$_\pi$L from 1.33 V · cm to 0.8 V · cm (see
191 Supplementary Section V). We estimate that the mode overlap for the unclad device is 0.016 %
192 and for the SU-8 clad device is 0.03 %, based on our simulations (see Methods). The Δn_{eff} for
193 the SU-8 clad device is almost double the Δn_{eff} extracted for an unclad device, in agreement
194 with the improvement in the mode overlap from our COMSOL computations. Considering the
195 relatively small mode overlap with the monolayer CVD WS$_2$ in this present work (0.03 %), one
196 could envision an even higher phase modulation efficiency using alternative waveguide
197 geometries with different degrees of mode confinement such as slot waveguides and photonic
198 crystals. We measure a 3 dB bandwidth of 0.3 GHz in our devices with minimal DC electrical
199 power dissipation of 0.64 nW in the WS$_2$-HfO$_2$-ITO capacitor (see Supplementary Section VI
200 and VII). The frequency response of the phase modulator is measured using a 40 GHz fast
201 photodiode and an electrical vector network analyzer (VNA) at 1550 nm. The bandwidth is
202 currently limited by the resistance of monolayer WS$_2$, and can be increased with improved
203 electrical contacts, optimized geometry, and control over the initial doping density.

205 Finally, we demonstrate that the gating induced electro-refractive effect extends to other
206 semiconductor TMDs by fabricating and characterizing a SiN-MoS$_2$ composite waveguide

207   embedded in a MZI structure (see figure 4a). The measured Δn_{eff} as a function of gate voltage is

208   shown in Figure 4b, and reaches a maximum of 6.4×10^{-4} (RIU) at 8 V (see Supplementary

209   Section VIII). The phase modulation efficiency $V_{\pi}L$ is 1.7 V • cm. Figure 4c compares the index

210   change (Δn) for MoS_2 and WS_2 with gate voltage. In both cases the index changes strongly, with

211   the change in WS_2 roughly double that MoS_2.

Figure 4 | **Phase tuning of monolayer MoS$_2$ in a composite SiN-MoS$_2$ waveguide and comparison of the** **|Δn/Δk| for different materials.** (a) Illustration of a composite SiN-MoS$_2$ waveguide, where the optical mode is shared between the waveguide and MoS$_2$. Figure right inset illustrates the optical mode profile for the composite SiN-MoS$_2$ waveguide, with an optical mode overlap of 0.054% with the monolayer MoS$_2$. (b) Change in the effective index (Δn_{eff}) of the propagating mode with voltage, extracted from the normalized MZI transmission

218   spectra of the composite SiN-MoS$_2$ waveguide (see Supplementary Section VIII). (c) Extracted change in refractive

219   index of the monolayer TMD's (Δn_{TMD}) such as WS$_2$ and MoS$_2$ with a voltage swing of 8 V across the TMD-HfO$_2$-

220   ITO capacitor. The error bars in the Δn calculations include the rms error in the effective index measurements from

221   Figure 3c and 4b, variation in the thickness of monolayer ($\pm$ 0.05 nm), and variation in the height of the cladding

222   oxide by about $\pm$ 25 nm included during the COMSOL simulations. (d) Comparison of |$\Delta n/\Delta k$| vs propagation length

223   (L = 1/α, where α is the insertion loss in 1/μm) for monolayer 2D materials (graphene[17,20], MoS$_2$[25] and WS$_2$[26]) and

224   bulk materials including Si[35–38] and III-V on Si (InGaAsP/Si hybrid MOS)[39] (see Supplementary Section X). The

225   earlier demonstrations measuring the tunable optical properties in 2D TMDs were performed using out of plane

226   techniques and were limited to the wavelength regime near or at their excitonic resonances. In order to compare the

227 |$\Delta n/\Delta k$| for 2D monolayers and bulk materials on the same graph, we assume in-plane propagation with a mode

228   overlap factor of 0.06% (similar to the one for the device in Figure 1) for all 2D materials.

229

230   The demonstrated strong light matter interaction in monolayer TMDs could open up doors for a

231   range of novel applications with these 2D materials and enable highly reconfigurable photonic

232   circuits with low optical loss and power dissipation. We show in figure 4d that the doping

233   induced |$\Delta n/\Delta k$| $\sim$ 125 for semiconductor monolayers at NIR wavelengths is significantly higher

234   than the |$\Delta n/\Delta k$| reported for 2D materials and various electro-refractive materials employed in

235   silicon photonics such as graphene[17,20] and silicon[35–38], while accompanied by comparatively

236   lower insertion loss (see Supplementary Section X). The high $\Delta n/\Delta k$ is due to the 2D

237   configuration in the composite platform that lends itself to extremely high doping of the material.

238   The low absorption in TMDs at such high doping densities is due to the limited phase space in a

239   lower dimensional system. The demonstrated composite waveguide platform (with V$_\pi$L of 0.8 V

240   $\cdot$ cm) already outperforms the current state of the art lithium niobate modulators – the gold

241   standard for current phase modulators (with V$_\pi$L of 1.8 – 2.4 V $\cdot$ cm)[40,41]. Traditional phase

242   modulators based on either thermo-optic or induced electro-optic $\chi^{(2)}$ effects have similar low

243   optical losses as our SiN-TMD device, but suffer from either high electrical power consumption

244   and low operation bandwidth[42–44] or require a large device footprint and requires complex

245   fabrication techniques[41,45,46], respectively. For large scale photonic systems, wafer scale

246   integration of TMD materials with silicon photonics can be done either as a direct TMD growth

247   process on silicon wafers[31,47,48], or as a post processing step where large wafer scale TMD films[49]

248   are transferred on a silicon photonics platform, fabricated in a standard foundry. The low

249   electrical power dissipation and moderate operation bandwidth in our SiN-TMD platform allows

250 for the large scale integration of these phase modulators in numerous applications such as
251 LIDAR, phased arrays, optical switching, quantum and optical neural networks.

References

253 1. Bonaccorso, F., Sun, Z., Hasan, T. & Ferrari, A. C. Graphene photonics and optoelectronics.
254 *Nat. Photonics* **4**, 611–622 (2010).

255 2. Wang, Q. H., Kalantar-Zadeh, K., Kis, A., Coleman, J. N. & Strano, M. S. Electronics and
256 optoelectronics of two-dimensional transition metal dichalcogenides. *Nat. Nanotechnol.* **7**,
257 699–712 (2012).

258 3. Santos, E. J. G. & Kaxiras, E. Electrically Driven Tuning of the Dielectric Constant in MoS2
259 Layers. *ACS Nano* **7**, 10741–10746 (2013).

260 4. Xia, F., Wang, H., Xiao, D., Dubey, M. & Ramasubramaniam, A. Two-dimensional material
261 nanophotonics. *Nat. Photonics* **8**, 899–907 (2014).

262 5. Ross, J. S. *et al.* Electrically tunable excitonic light-emitting diodes based on monolayer
263 WSe2 p-n junctions. *Nat. Nanotechnol.* **9**, 268–272 (2014).

264 6. Jariwala, D., Sangwan, V. K., Lauhon, L. J., Marks, T. J. & Hersam, M. C. Emerging Device
265 Applications for Semiconducting Two-Dimensional Transition Metal Dichalcogenides. *ACS*
266 *Nano* **8**, 1102–1120 (2014).

267 7. Schwarz, S. *et al.* Two-Dimensional Metal–Chalcogenide Films in Tunable Optical
268 Microcavities. *Nano Lett.* **14**, 7003–7008 (2014).

269 8. C. Ferrari, A. *et al.* Science and technology roadmap for graphene, related two-dimensional
270 crystals, and hybrid systems. *Nanoscale* **7**, 4598–4810 (2015).

271 9. Pospischil, A. & Mueller, T. Optoelectronic Devices Based on Atomically Thin Transition
272 Metal Dichalcogenides. *Appl. Sci.* **6**, 78 (2016).

273 10. Mak, K. F. & Shan, J. Photonics and optoelectronics of 2D semiconductor transition metal
274 dichalcogenides. *Nat. Photonics* **10**, 216–226 (2016).

275 11. Xiao, J., Zhao, M., Wang, Y. & Zhang, X. Excitons in atomically thin 2D semiconductors
276 and their applications. *Nanophotonics* **6**, 1309–1328 (2017).

277 12. Manzeli, S., Ovchinnikov, D., Pasquier, D., Yazyev, O. V. & Kis, A. 2D transition metal
278 dichalcogenides. *Nat. Rev. Mater.* **2**, 17033 (2017).

279 13. Bernardi, M., Ataca, C., Palummo, M. & Grossman, J. C. Optical and Electronic Properties
280 of Two-Dimensional Layered Materials. *Nanophotonics* **6**, 479–493 (2016).

281   14. Bie, Y.-Q. *et al.* A MoTe$_2$-based light-emitting diode and photodetector for silicon photonic
282   integrated circuits. *Nat. Nanotechnol.* **12**, 1124–1129 (2017).

283   15. Basov, D. N., Averitt, R. D. & Hsieh, D. Towards properties on demand in quantum
284   materials. *Nat. Mater.* **16**, 1077–1088 (2017).

285   16. Romagnoli, M. *et al.* Graphene-based integrated photonics for next-generation datacom and
286   telecom. *Nat. Rev. Mater.* **3**, 392 (2018).

287   17. Woessner, A. *et al.* Electrical 2π phase control of infrared light in a 350-nm footprint using
288   graphene plasmons. *Nat. Photonics* **11**, 421–424 (2017).

289   18. Mohsin, M. *et al.* Experimental verification of electro-refractive phase modulation in
290   graphene. *Sci. Rep.* **5**, 10967 (2015).

291   19. Ding, Y. *et al.* Effective Electro-Optical Modulation with High Extinction Ratio by a
292   Graphene–Silicon Microring Resonator. *Nano Lett.* **15**, 4393–4400 (2015).

293   20. Sorianello, V. *et al.* Graphene–silicon phase modulators with gigahertz bandwidth. *Nat.*
294   *Photonics* **12**, 40–44 (2018).

295   21. Phare, C. T., Lee, Y.-H. D., Cardenas, J. & Lipson, M. Graphene electro-optic modulator
296   with 30 GHz bandwidth. *Nat. Photonics* **9**, 511–514 (2015).

297   22. Ross, J. S. *et al.* Electrical control of neutral and charged excitons in a monolayer
298   semiconductor. *Nat. Commun.* **4**, 1474 (2013).

299   23. Chernikov, A. *et al.* Electrical Tuning of Exciton Binding Energies in Monolayer WS$_2$. *Phys.*
300   *Rev. Lett.* **115**, 126802 (2015).

301   24. Wang, G. *et al.* Colloquium: Excitons in atomically thin transition metal dichalcogenides.
302   *Rev. Mod. Phys.* **90**, 21001 (2018).

303   25. Mak, K. F. *et al.* Tightly bound trions in monolayer MoS$_2$. *Nat. Mater.* **12**, 207–211 (2013).

304   26. Yu, Y. *et al.* Giant Gating Tunability of Optical Refractive Index in Transition Metal
305   Dichalcogenide Monolayers. *Nano Lett.* **17**, 3613–3618 (2017).

306   27. Doylend, J. K. *et al.* Two-dimensional free-space beam steering with an optical phased array
307   on silicon-on-insulator. *Opt. Express* **19**, 21595–21604 (2011).

308   28. Sun, J., Timurdogan, E., Yaacobi, A., Hosseini, E. S. & Watts, M. R. Large-scale
309   nanophotonic phased array. *Nature* **493**, 195–199 (2013).

310   29. Shen, Y. *et al.* Deep learning with coherent nanophotonic circuits. *Nat. Photonics* **11**, 441–
311   446 (2017).

312　30. Miller, S. A. *et al.* 512-Element Actively Steered Silicon Phased Array for Low-Power
313　　　LIDAR. in *Conference on Lasers and Electro-Optics (2018), paper JTh5C.2* JTh5C.2
314　　　(Optical Society of America, 2018).

315　31. Kang, K. *et al.* High-mobility three-atom-thick semiconducting films with wafer-scale
316　　　homogeneity. *Nature* **520**, 656–660 (2015).

317　32. Braga, D., Gutiérrez Lezama, I., Berger, H. & Morpurgo, A. F. Quantitative Determination
318　　　of the Band Gap of WS2 with Ambipolar Ionic Liquid-Gated Transistors. *Nano Lett.* **12**,
319　　　5218–5223 (2012).

320　33. Li, Y. *et al.* Measurement of the optical dielectric function of monolayer transition-metal
321　　　dichalcogenides: MoS_2, $MoSe_2$, WS_2, and WSe_2. *Phys. Rev. B* **90**, 205422 (2014).

322　34. Mlack, J. T. *et al.* Transfer of monolayer TMD WS_2 and Raman study of substrate effects.
323　　　*Sci. Rep.* **7**, 43037 (2017).

324　35. Akiyama, S. *et al.* 12.5-Gb/s operation with 0.29-V·cm $V_\pi L$ using silicon Mach-Zehnder
325　　　modulator based-on forward-biased pin diode. *Opt. Express* **20**, 2911–2923 (2012).

326　36. Liu, A. *et al.* A high-speed silicon optical modulator based on a metal–oxide–semiconductor
327　　　capacitor. *Nature* **427**, 615–618 (2004).

328　37. Marris-Morini, D. *et al.* Low loss and high speed silicon optical modulator based on a lateral
329　　　carrier depletion structure. *Opt. Express* **16**, 334–339 (2008).

330　38. Xiao, X. *et al.* High-speed, low-loss silicon Mach–Zehnder modulators with doping
331　　　optimization. *Opt. Express* **21**, 4116–4125 (2013).

332　39. Han, J.-H. *et al.* Efficient low-loss InGaAsP/Si hybrid MOS optical modulator. *Nat.*
333　　　*Photonics* **11**, 486–490 (2017).

334　40. Wang, C. *et al.* Integrated lithium niobate electro-optic modulators operating at CMOS-
335　　　compatible voltages. *Nature* **562**, 101 (2018).

336　41. Wang, C., Zhang, M., Stern, B., Lipson, M. & Lončar, M. Nanophotonic lithium niobate
337　　　electro-optic modulators. *Opt. Express* **26**, 1547–1555 (2018).

338　42. Harris, N. C. *et al.* Efficient, compact and low loss thermo-optic phase shifter in silicon. *Opt.*
339　　　*Express* **22**, 10487–10493 (2014).

340　43. Masood, A. *et al.* Fabrication and characterization of CMOS-compatible integrated tungsten
341　　　heaters for thermo-optic tuning in silicon photonics devices. *Opt. Mater. Express* **4**, 1383–
342　　　1388 (2014).

343 44. Chang, Y.-C., Roberts, S. P., Stern, B. & Lipson, M. Resonance-Free Light Recycling.
344   (2017).

345 45. Timurdogan, E., Poulton, C. V., Byrd, M. J. & Watts, M. R. Electric field-induced second-
346   order nonlinear optical effects in silicon waveguides. *Nat. Photonics* **11**, 200–206 (2017).

347 46. Kieninger, C. *et al.* Ultra-high electro-optic activity demonstrated in a silicon-organic hybrid
348   modulator. *Optica* **5**, 739–748 (2018).

349 47. Elías, A. L. *et al.* Controlled Synthesis and Transfer of Large-Area WS2 Sheets: From Single
350   Layer to Few Layers. *ACS Nano* **7**, 5235–5242 (2013).

351 48. McCreary, K. M., Hanbicki, A. T., Jernigan, G. G., Culbertson, J. C. & Jonker, B. T.
352   Synthesis of Large-Area WS_2 monolayers with Exceptional Photoluminescence. *Sci. Rep.* **6**,
353   19159 (2016).

354 49. Lee, J. *et al.* Crack-Release Transfer Method of Wafer-Scale Grown Graphene Onto Large-
355   Area Substrates. *ACS Appl. Mater. Interfaces* **6**, 12588–12593 (2014).

356

372

Author contributions: I.D. and M.L. conceived and proposed the TMD based photonic design and experiments. S.H.C, J.H. and D.N.B proposed the use of WS$_2$ for these photonic structures. C.P. and J.P. provided the MOCVD WS$_2$ film for the ionic liquid experiments, Y.Y. and L.C. provided the CVD WS$_2$ and MoS$_2$ film for the capacitive device experiments, and S.H.C and B.L. performed the TMD transferring and characterization (PL measurements). I.D. fabricated the composite photonic device, with assistance from S.H.C for TMD processing and development, G.R.B for the ITO development and M.A.T for the SU-8 cladding of the composite structures. I.D. performed and analyzed the optical measurements of the photonic devices. I.D. and G.R.B performed the capacitance measurement of these structures. I.D. and M.L. prepared the manuscript. S.H.C, D.N.B, J.H. and M.L. edited the manuscript. J.H. and M.L. supervised the project.

Corresponding author: Correspondence to Michal Lipson

Methods

Device Fabrication.

TMD preparation, transfer and patterning- The PMMA/TMD stack was delaminated from the SiO$_2$/Si substrate by floating in a hot 1 M KOH solution with the PMMA side up. The PMMA/TMD stack is then rinsed in water a couple of times, before transferring it onto the SiN waveguides. After the transfer, the TMD clad waveguides are left to dry for a few hours before the PMMA was removed by soaking in acetone and rinsing in isopropanol. The transferred TMD is then patterned with HSQ/PMMA stack using electron beam lithography (EBL), followed by oxygen plasma and CHF$_3$/O$_2$ for etching residual PMMA and TMD. After the transfer, the TMD clad waveguides are left to dry for a few hours before the PMMA was removed by soaking in acetone and rinsing in isopropanol. The transferred TMD is then patterned with HSQ/PMMA stack using electron beam lithography (EBL), followed by oxygen plasma and CHF$_3$/O$_2$ for etching residual PMMA and TMD.

Device Fabrication for SiN-TMD Ionic Liquid Photonic Devices. We lithographically defined 1.3 μm wide waveguides on 330 nm high Silicon nitride (SiN), deposited using Low Pressure Chemical Vapor Deposition (LPCVD) at 800 ^{o}C and annealed at 1200 ^{o}C for 3 hours, on 4 μm thermally oxidized SiO_2, with a combination of e-beam lithography to define the waveguides and deep UV lithography to pattern the CMP marks. We etch the SiN waveguides and CMP patterns using CHF_3/O_2 chemistry in Oxford 100 Plasma ICP RIE, followed by the deposition of 600 nm of Plasma Enhanced Chemical Vapor Deposition (PECVD) silicon dioxide (SiO_2) on the waveguides. We planarize the SiO_2 to about 100 nm above the SiN waveguides using standard chemical planarization (CMP) techniques to create a planar surface for the transfer of the MOCVD WS_2 monolayer and to prevent the TMD film from breaking at the waveguide edges. The power splitter (combiner) at the input (output) of the MZI structure is designed using a 1×2 (2×1) multimode interferometer (MMI). Due to the disproportionate ratio of the height (330 nm) to the width (1.3 μm) of the waveguide and sensitivity of the MMI structure, the MZI supports wavelength fringes from 1520 – 1630 nm for the TE mode and 1455 – 1480 nm for the TM mode. Following the TMD preparation, transfer and patterning mentioned above, the metal contacts are lithographically patterned using the DUV mask aligner and 50/80 nm of Ti/Au is deposited using electron beam evaporation, followed by liftoff in acetone.

Device Fabrication for SiN-TMD Capactitive Devices. We lithographically defined 1 μm wide waveguides on 360 nm high Silicon nitride (SiN), deposited using Low Pressure Chemical Vapor Deposition (LPCVD) at 800 ^{o}C and annealed at 1200 ^{o}C for 3 hours, on 4 μm thermally oxidized SiO_2, using 248 nm deep ultraviolet lithography. We etch the SiN waveguides using CHF_3/O_2 chemistry in Oxford 100 Plasma ICP RIE, followed by the deposition of 600 nm of Plasma Enhanced Chemical Vapor Deposition (PECVD) silicon dioxide (SiO_2) on the waveguides. We planarize the SiO_2 to about 260 nm {40 nm} above the SiN waveguides using standard chemical planarization (CMP) techniques to create a planar surface for the transfer of the WS_2 {MoS_2} monolayer and to prevent the TMD film from breaking at the waveguide edges. The 260 {40 nm} nm SiO_2 layer prevents the lossy ITO layer of the capacitor from interacting with the optical mode too strongly. A 45 nm {5 nm} of thermal ALD alumina is deposited on top of SiO_2 to isolate the waveguides from the subsequent fabrication steps for the TMD-HfO_2-ITO capacitor. The TMD is prepared, transferred and patterned using the aforementioned process. The metal

433   contacts to the TMD layer are then patterned using EBL and 30 nm Ti/ 50 nm Au is deposited

434   using electron beam evaporation, followed by lift-off in acetone. 26 nm {37 nm} of thermal

435   ALD Hafnia at 200 °C is then deposited to form the dielectric for the TMD-HfO$_2$-ITO capacitor.

436   The other electrode of the capacitor is first patterned using EBL and then Indium Tin oxide

437   (ITO) is sputtered at room temperature (24 °C), at a chamber base pressure of 12 mTorr, with an

438   Argon flow of 30 sccm and 5 sccm oxygen flow, followed by lift-off in acetone. To reduce the

439   resistivity of the sputtered ITO film, the substrate is heated to a temperature of 200°C and

440   annealed in vacuum with the chamber pressure at 10^{-6} Torr, and an oxygen flow of 5 sccm for 30

441   minutes. We characterize the complex refractive index of ITO and thereby its doping using

442   visible and infrared ellipsometry (Woollam VASE) and fit to a Drude-Lorentz relation (see

443   Supplementary Section XI). Finally, the metal contacts to the ITO layer are patterned using EBL

444   and 30nm Ti/ 50 nm Au is then deposited using e-beam evaporation, followed by lift-off in

445   acetone. To define devices with SU-8 on the composite SiN-WS$_2$ waveguides, SU-8 is

446   photolithographically patterned on the waveguide and developed, by spinning SU-8 to a

447   thickness of 3.5 μm.

448

449   Note. The numbers in curly brackets {} indicate the dimensions for the composite SiN-MoS$_2$

450   devices.

451

452   **Experimental Setup.** We couple TE/TM polarized light from a tunable NIR laser (1450 nm –

453   1600 nm) to the SiN microring/MZI input using a tapered single mode fiber, which is then

454   collected at the SiN bus/MZI output, using a similar tapered fiber. We record the microring/MZI

455   transmission spectrum for different DC bias voltages applied across the WS$_2$-HfO$_2$-ITO

456   capacitor, to measure the phase shift and absorption change. We normalize each of the MZI/ring

457   transmission spectra first by the maximum output power across the measured wavelength range

458   and then by the optical power spectral profile measured at the output of one of the MZI arms by

459   coupling light to a similar SiN waveguide with only one MMI splitter at the input of MZI. The

460   above normalization process eliminates the wavelength dependent optical loss experienced by

461   the incident laser light in the tapered optical fiber, the fiber polarizer, SiN waveguide and the

462   MMI, which are all designed to operate optimally at 1550 nm with the TE polarization. It also

463   accounts for the wavelength dependent power fluctuations of the laser, if any.

464   For small-signal RF bandwidth measurement using the Vector Network Analyzer (VNA),

465   we apply a DC bias voltage of 0 V across the WS_2-HfO_2-ITO capacitor, combined with an RF

466   signal of -10 dBm with a source impendance of 50 Ω.

467

468   **Optical Sheet Conductivity of Monolayer TMD.** We use the 2D sheet conductivity model to

469   extract the Δn_{WS2} and Δk_{WS2}, as is commonly done when modeling graphene monolayers[42]. We

470   extract the complex index change of the monolayer ($\Delta n + i\Delta k$) with carrier densities by

471   comparing the measured Δn_{eff} and Δk_{eff} (Figure 1e)), with the simulated change obtained using

472   COMSOL Multiphysics finite element model (FEM). We model the monolayer TMD as a

473   conductive sheet with a surface charge density ($J = \sigma_s \cdot E$) and complex optical conductivity[43]

474    $\sigma_s = \sigma_R + j\sigma_I$. $\sigma_s(\omega)$ is related to the dielectric permittivity ($\varepsilon(\omega)$) through the equation

475                               $$\sigma_s(\omega) = j\omega t_d \varepsilon_0 \left(\varepsilon(\omega) - 1\right) \qquad (1)$$

476   where, t_d defines the thickness of the monolayer TMD (0.85 nm $\pm$ 0.05 nm)[21]. We estimate the

477   complex index change of the monolayer from the computed change in conductivity ($\Delta\sigma$) using

478   the equation

479                        $$\sigma_s(\omega) + \Delta\sigma = j\omega t_d \varepsilon_0 \left(\varepsilon(\omega) + \Delta\varepsilon - 1\right) \qquad (2)$$

480   Where, $\Delta\varepsilon$ defines the change in dielectric permittivity ($\varepsilon(\omega)$), which is related to Δn and

481   Δk through

482                      $$\varepsilon(\omega) + \Delta\varepsilon = (n + \Delta n + i(k + \Delta k))^2 \qquad (3).$$

483   The change in the real part of effective index of the mode (Δn_{eff}) signifies a change in the

484   imaginary part of the optical conductivity ($\Delta\sigma_I$), whereas the change in the imaginary part of the

485   effective index (Δk_{eff}) of the mode is reflected in the real part of the optical conductivity ($\Delta\sigma_R$)

486   through equation (1), (2) and (3). Since the change in complex effective index of the composite

487   SiN-WS_2 waveguide is contingent on the spatial overlap between the propagating optical mode

488   and the monolayer WS_2, the true measure of the efficiency of the phase modulation lies in the

489   change of its in-plane optical sheet conductivity (S) and thereby its real and imaginary part of the

490   refractive index ($\Delta n + i\Delta k$) with electrostatic gating. We calculate ($\Delta n_{WS2} + i\Delta k_{WS2}$) by

491   modeling the monolayer as a boundary condition with surface current density ($J = \sigma_s \cdot E$), which

492   eliminates the approximation of the thickness of the monolayer in our COMSOL model.

493   We quantify the mode overlap by replacing the surface current density ($J = \sigma \cdot E$) in the

494   refractive index calculations, with a monolayer thickness (t_d) of 0.85 $\pm$ 0.05 nm thickness, and

495   finding the surface integral to fraction of the energy flux (E × H) of the mode in monolayer WS_2,

496   compared to the total mode flux in the composite waveguide.

497

498   **Comparison of the electro-refractive change in WS_2 and MoS_2** - Even though the Δn_{eff} for

499   the air clad SiN-WS_2 composite waveguide (Figure 3c) is similar to the Δn_{eff} of the air clad SiN-

500   MoS_2 (Figure 4a), the extracted Δn_{WS2} is higher than Δn_{Mos2}, due to the lower optical mode

501   overlap of 0.016 % in the SiN-WS_2 waveguide, as compared to that of SiN-MoS_2 waveguide.

502

503   **Data availability -** The experimental dataset and its analysis is provided in the paper and any

504   additional dataset, if required, is available from the corresponding authors upon reasonable

505   request.